Extended main sequence turnoffs in open clusters as seen by *Gaia* – I. NGC 2818 and the role of stellar rotation

N. Bastian,[1][*] S. Kamann,[1] I. Cabrera-Ziri,[2][†] C. Georgy,[3] S. Ekström,[3] C. Charbonnel,[3,4] M. de Juan Ovelar[1] and C. Usher[1]

[1]*Astrophysics Research Institute, Liverpool John Moores University, 146 Brownlow Hill, Liverpool L3 5RF, UK*
[2]*Harvard-Smithsonian Center for Astrophysics, 60 Garden Street, Cambridge, MA 02138, USA*
[3]*Department of Astronomy, University of Geneva, Chemin des Maillettes 51, CH-1290, Versoix, Switzerland*
[4]*IRAP, UMR 5277, CNRS and Université de Toulouse, 14, avenue douard Belin, F-31400 Toulouse, France*

ABSTRACT

We present an analysis of the relatively low mass ($\sim$2400 M$_\odot$), $\sim$800 Myr, Galactic open cluster, NGC 2818, using *Gaia* DR2 results combined with VLT/FLAMES spectroscopy. Using *Gaia* DR2 proper motions and parallax measurements, we are able to select a clean sample of cluster members. This cluster displays a clear extended main sequence turn-off (eMSTO), a phenomenon previously studied mainly in young and intermediate age massive clusters in the Magellanic clouds. The main sequence of NGC 2818 is extremely narrow, with a width of $\sim$0.01 magnitudes ($G_{\rm BP}$–$G_{\rm RP}$), suggesting very low levels of differential extinction. Using VLT/FLAMES spectroscopy of 60 cluster members to measure the rotational velocity of the stars ($V \sin i$), we find that stars on the red side of the eMSTO have high $V \sin i$ ($>160\,\mathrm{km\,s^{-1}}$) while stars on the blue side have low $V \sin i$ ($<160\,\mathrm{km\,s^{-1}}$), in agreement with model predictions. The cluster also follows the previously discovered trend between the age of the cluster and the extent of the eMSTO. We conclude that stellar rotation is the likely cause of the eMSTO phenomenon.

Key words: stars: rotation – open clusters and associations: individual: NGC 2818 – galaxies: star clusters: general.

1 INTRODUCTION

The extended main sequence turn-off (eMSTO) phenomenon is an observational feature that has been found in young and intermediate age (up to $\sim$2 Gyr) clusters in the Large and Small Magellanic clouds, where the MSTO of the cluster in colour-magnitude diagrams is more extended than would be expected for a simple stellar population (after accounting for binaries, extinction, and photometric uncertainties). The origin of the eMSTO feature was initially suggested to be due to a large age spread (hundreds of Myr) within these clusters (e.g. Mackey & Broby Nielsen 2007; Milone et al. 2009; Goudfrooij et al. 2014), although subsequent work has shown that a stellar evolutionary effect, likely stellar rotation, was the most probable cause (e.g. Bastian & de Mink 2009; Brandt & Huang 2015b; Niederhofer et al. 2015; Cabrera-Ziri et al. 2016). Actual age spreads, as the origin of the eMSTO, are disfavoured due to the observed relation between the extent of the inferred age spread

and the age of the clusters (Niederhofer et al. 2015).[1] Spectroscopic studies of stars on the eMSTO in these clusters have found evidence that indeed stellar rotation is directly linked to the position within the MSTO (Dupree et al. 2017; Kamann et al. 2018; Marino et al. 2018).

There have been suggestions that the width of the eMSTO is linked to the cluster mass, with higher mass clusters displaying broader spreads (e.g. Conroy & Spergel 2011; Goudfrooij et al. 2014). However, the eMSTO feature has been found in clusters with masses down to 2–5 $\times$ 10^3 M$_\odot$ (Piatti & Bastian 2016), and statistical analyses found that cluster age had a much larger correlation with eMSTO widths than mass (Niederhofer et al. 2016). Recent work by Martocchia et al. (2018) found that NGC 1978, a massive ($\sim$3 $\times$ 10^5 M$_\odot$), 2 Gyr cluster does not host an eMSTO, adding further support that age, and not mass, is the controlling parameter (see also Georgy et al., in prep.).

Most studies of eMSTOs in clusters have focussed on massive LMC/SMC clusters with *Hubble Space Telescope* observations tak-

---

[1] See Bastian & Lardo (2018) for further discussion of the evidence against actual age spreads within massive clusters.
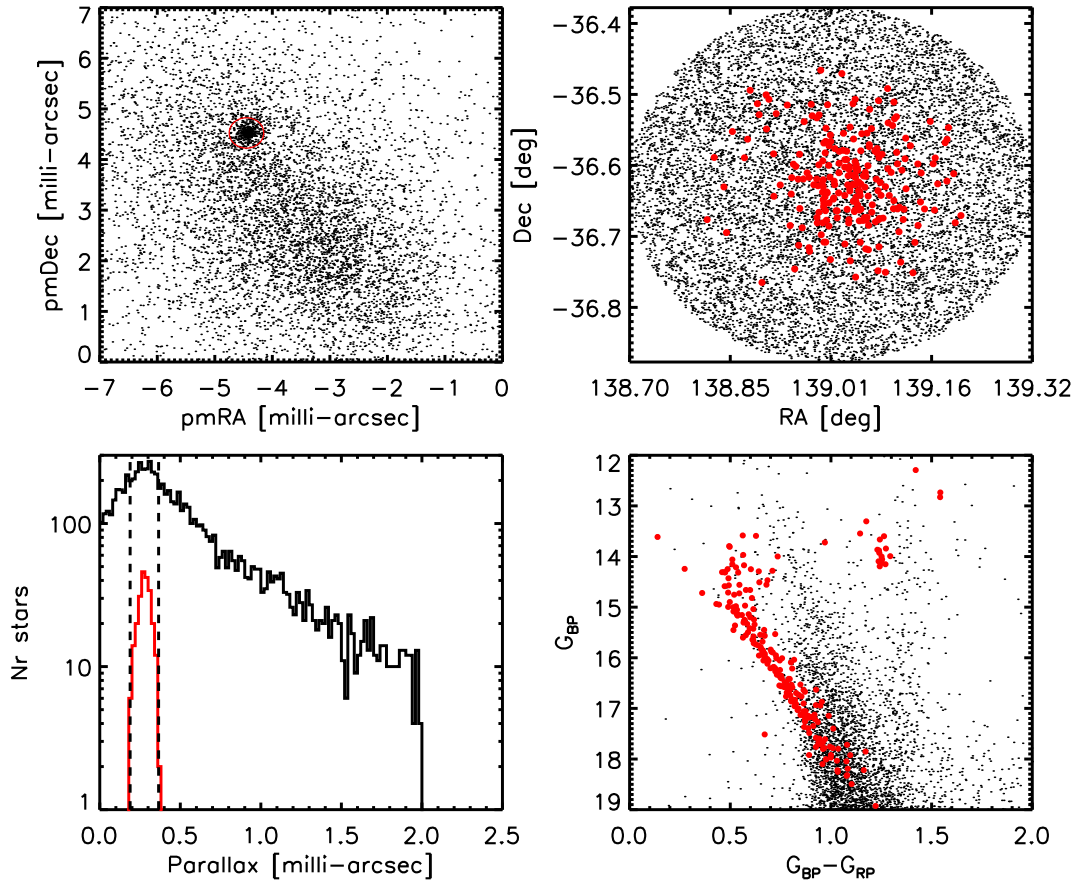
Figure 1. Upper left: Proper motion of all stars in the *Gaia* catalogue within 15' of the centre of NGC 2818. A clear overdensity of points belonging to cluster is seen. The circle shows the first selection of cluster members. **Upper right:** The spatial distribution of all stars selected with cluster members highlight as filled (red) points. **Bottom left:** The parallax distribution of all stars (upper curve, black) and selected cluster members (lower curver, red). The vertical dashed lines show the cuts applied to select cluster members. **Bottom right:** The CMD (in *Gaia* blue and red passbands) of all stars in the field (points) and cluster members (filled red circles). An extended main sequence turn-off is clearly visible at $G_{BP} \approx 14.5$ mag.

ing advantage of the lack of background/foreground confusion, high membership probabilities, and large numbers of stars on the MSTO (10s–100s) that allow statistical analyses. While there have been some attempts to find and study the eMSTO phenomenon in open clusters in the Galaxy (e.g. Brandt & Huang 2015a), such studies have been limited due to the low number of stars on the MSTO, or in the case of Trumpler 20 (Platais et al. 2012) no eMSTO was found (once differential extinction was taken into account). There have been previous suggestions in open clusters that a dual or extended main sequence turn-off could be due to rapid rotators within the clusters (Twarog 1983; Twarog et al. 2015). If clean samples of cluster members can be found in open clusters, it opens the way for detailed follow-up studies, as these stars are 3–8 magnitudes brighter than their LMC/SMC counterparts. Additionally, by studying Galactic open clusters, the role of metallicity can be explored as, to date, only SMC/LMC metallicity environments have been studied.

Gaia DR2 (Gaia Collaboration et al. 2016, 2018) has opened the possibility of an entirely new perspective on the problem, by allowing the study of eMSTOs (and the related phenomenon of split main-sequences – e.g. Milone et al. 2016) in relatively low mass ($\lesssim 3000$ M$_\odot$) open clusters in the Galaxy. This is due to the ability to select extremely clean samples of cluster members, mitigating the effects of contamination from fore/back-ground stars.

In this paper, we exploit *Gaia* DR2 and archival VLT/FLAMES spectroscopy to discover and analyse the eMSTO in the ~800–900 Myr open cluster, NGC 2818. This is a first in a series of papers focussed on the eMSTO phenomenon in open clusters.

2 OBSERVATIONS AND METHODS

2.1 Selection of cluster members

We searched the *Gaia* DR database for all sources within 12' of the centre of NGC 2818 (Gaia Collaboration et al. 2016, 2018). We then looked at the resulting proper motion map of these stars and a clear overdensity could be seen at pmRA = −4.425 and pmDec = 4.532 (top left-hand panel of Fig. 1). We used all stars with proper motion values of 0.3 milli-arcseconds of this centre for our first selection. These stars showed a clear peak in the parallax distribution at 0.281 milli-arcseconds, corresponding to a distance of 3.56 kpc which we will adopt throughout this work.[2] We then made a further selection in parallax, $0.1885 \leq$ parallax ≤ 0.365 (shown as the vertical dashed lines in the lower left-hand panel of Fig. 1) and applied a radial cut of 10' to obtain our final member sample. Their spatial

---

[2]This does not include the −0.029 milli-arsecond zeropoint offset found by Lindegren et al. (2018) for Quasars in DR2.

Table 1. Properties of the selected cluster candidate using the position, Plx and proper motions. The full table can be found in the electronic version of the article.

RA [deg]	Dec [deg]	Plx [mas]	ePlx [mas]	PMRA [mas yr⁻¹]	ePMRA [mas yr⁻¹]	PMDec [mas yr⁻¹]	ePMDec [mas yr⁻¹]	G_{BP} [mag]	eG$_{BP}$ [mag]	G_{RP} [mag]	eG$_{RP}$ [mag]
139.012145996	−36.627246857	0.3272	0.1053	−4.5730	0.1370	4.3370	0.1520	17.5141	0.0124	16.8432	0.0088
139.011337280	−36.622184753	0.2156	0.0602	−4.4820	0.0800	4.5960	0.0910	16.7621	0.0068	15.9852	0.0088
138.994445801	−36.629962921	0.2465	0.0542	−4.4080	0.0730	4.5830	0.0850	16.5474	0.0047	15.8035	0.0030
139.004837036	−36.616539001	0.2818	0.0355	−4.4410	0.0470	4.4300	0.0560	16.0921	0.0033	15.2908	0.0024

distribution and colour-magnitude diagrams (using the blue and red passband photometry from *Gaia*) are shown in the top-right-hand and bottom-right-hand panels of Fig. 1, respectively.[3]

As already evident from Fig. 1, NGC 2818 displays a clear extended main sequence turn-off. A list of selected members is given in Table 1.

2.2 Rotational velocities

Spectroscopic observations of main-sequence (MS) and turn-off (TO) stars in NGC 2818 are publicly available in the ESO archive. Observations were conducted in 2014 March using the GIRAFFE multi-object spectrograph in its MEDUSA mode under the programme 093.D-0868(A) (PI: Simunovic). The employed setups are HR05 and HR09 that offer a nominal resolution of $R \sim 20\,250$ and 18 000 at the central wavelengths of 4471 and 5258 Å, respectively. Stars were observed for 2×45 min in each grating, leading to a signal-to-noise (S/N) of $\sim$100 and $\sim$20 (per single exposure) for the brightest and the faintest star in the sample, respectively. We retrieved the extracted, wavelength-calibrated, one-dimensional (1D) spectra from the Phase 3 ESO archive. The reduced MEDUSA 1D-spectra come with error estimates and signal-to-noise ratio per wavelength bin and the wavelength scale is in the heliocentric reference system. A total of 60 stars from 093.D-0868(A) are included in the *Gaia* DR2 photometric catalogue, and are shown in Fig. 2.

To determine rotational velocities, we performed a χ^2 minimization procedure between synthetic and the observed spectra. Atmospheric parameters were derived as follows. We adopted the effective temperatures, T_{eff}, from *Gaia* DR2. Surface gravities were derived from DR2 parallaxes, using the fundamental relation:

$$\log\left(\frac{g}{g_\odot}\right) = \log\left(\frac{M}{M_\odot}\right) + 4\log\left(\frac{T_{eff}}{T_\odot}\right) - \log\left(\frac{L}{L_\odot}\right)$$

We use V magnitudes from Stetson (2000),[4] bolometric corrections are based on Flower (1996) and Torres (2010), and solar magnitudes from Bessell, Castelli & Plez (1998). The masses were set to 1.6 M$_\odot$ and the resolution is set to the nominal HR05 and HR09. Micro-turbulence (ξt) is derived using the relation in Tsantaki et al. (2013) and macroturbulence is from Doyle et al. (2014). We adopt a metallicity of [Fe/H] = 0.0. All atmospheric parameters were kept fixed in our analysis and we allowed only $V\sin i$ to vary in our χ^2 minimization procedure.

The synthetic spectra were computed with the plane-parallel, local thermodynamic equilibrium (LTE) code MOOG (Sneden 1973; Sneden et al. 2012). The model atmospheres were calculated with the ATLAS9; starting from the grid of models available at F.
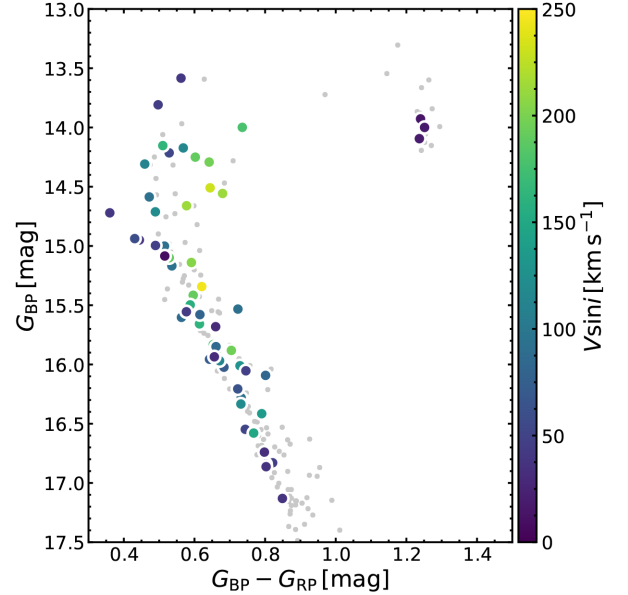
Figure 2. The CMD of NGC 2818 with colour-coding showing the measured $V\sin i$ of each star. Rapidly rotating stars preferentially lie on the red side of the eMSTO while slower rotating stars tend to be on the blue side, consistent with expectations if rotation is the cause of the eMSTO phenomenon.

Castelli's website.[5] When HR05 and HR09 spectra were available, we consider the final rotational velocity as the mean value measured from the two settings.

We calibrated the uncertainties of our $V\sin i$ measurements by using the stars with measurements in both gratings. When normalized by the squared sum of the uncertainties, the differences between the gratings should be normally distributed with a standard deviation of 1. To achieve this, a correction factor of 0.36 had to be applied to all uncertainties.

In Fig. 2, we show the CMD of cluster members along with the measured $V\sin i$ for the subsample of 60 members. Light blue represents rapid rotators while dark blue/black shows more slow rotators. It is evident that the rapid rotators preferentially lie to the red of the MSTO, whereas the slower rotators lie closer to the blue nominal main sequence. This is consistent with observations of young (Dupree et al. 2017) and intermediate age (Kamann et al. 2018) massive clusters in the LMC/SMC. We will quantitatively compare our observations with model predictions including rotation in Section 3.2. The properties of cluster members with $V\sin i$ measurements are listed in Table 2.

---

[3] A list with the photometric properties of all stars selected with the above criteria is available through the electronic journal website.
[4] http://www.cadc-ccda.hia-iha.nrc-cnrc.gc.ca/en/community/STETSON/standards/

[5] http://www.oact.inaf.it/castelli/

Table 2. Properties of the stars with *Vsini* measurements. The magnitudes are for the *Gaia* blue band pass (G_{BP}) and *Gaia* red band pass (G_{RP}). We list three *Vsini* values, $Vsini_{HR09}$ is that determined from the HR09 grating, $Vsini_{HR05}$ is from the HR05 grating, and the $V_{adopted}$ is the adopted value. '0.0' values denote stars where a measurement was possible in that grating. Errors on the photometry are not given, as they are generally <0.01 mag.

Gaia DR2 ID	RA [deg]	Dec [deg]	G_{BP} [mag]	G_{RP} [mag]	$Vsini_{HR09}$ [mag]	$eVsini_{HR09}$ [mag]	$Vsini_{HR05}$ [km s^{-1}]	$eVsini_{HR05}$ [km s^{-1}]	$Vsini_{adopted}$ [km s^{-1}]	$eVsini_{adopted}$ [km s^{-1}]
5623333339867028096	139.044769287	−36.650726318	15.68	15.02	31.0	2.8	0.0	0.0	31.0	2.8
5623333305507502720	139.018203735	−36.63874054	13.81	13.31	44.0	4.9	44.0	4.0	44.0	3.6
5623339318459536384	139.059326172	−36.609886169	14.95	14.51	0.0	0.0	39.0	3.7	39.0	3.7
5623380378350117504	139.036895752	−36.613384247	13.93	12.69	14.0	1.5	0.0	0.0	14.0	1.5
5623380442769067520	139.01902771	−36.597003937	14.09	12.86	19.0	1.2	17.0	0.9	17.7	0.9
5623386528743281408	139.012268066	−36.576229095	14.00	12.75	17.0	1.2	0.0	0.0	17.0	1.2
5623339352821216896	139.063354492	−36.600475311	15.53	14.81	91.0	7.3	0.0	0.0	91.0	7.3
5623333339867029120	139.040908813	−36.650588989	14.56	13.88	224.0	22.6	201.0	16.5	209.0	15.5
5623332858830717440	138.984985352	−36.673389435	14.51	13.87	231.0	26.9	0.0	0.0	231.0	26.9
5623386631822488832	139.025756836	−36.554733276	16.28	15.55	92.0	8.0	0.0	0.0	92.0	8.0
5623386563103010560	139.041259766	−36.562767029	14.00	13.26	187.0	19.0	170.0	14.1	176.0	13.2
5623380786366456448	138.928314209	−36.62758255	14.29	13.65	204.0	25.4	190.0	19.6	195.2	18.1
5623339249742007808	139.060165405	−36.615459442	16.83	16.02	42.0	2.8	40.0	2.8	41.0	2.3
5623338974864103808	139.083496094	−36.642276764	16.83	16.01	46.0	3.7	44.0	4.0	45.1	3.2
5623386391304315904	139.065444946	−36.570781708	15.15	14.62	118.0	14.4	107.0	15.0	112.7	12.3
5623339455900419840	139.080383301	−36.585018158	14.21	13.69	53.0	6.1	0.0	0.0	53.0	6.1
5623339455900421248	139.080383301	−36.588939667	14.25	13.65	190.0	26.3	0.0	0.0	190.0	26.3
5623339176724479232	139.094100952	−36.604549408	16.74	15.94	34.0	3.4	0.0	0.0	34.0	3.4
5623386253865372288	139.045028687	−36.598823547	14.59	14.11	0.0	0.0	92.0	11.6	92.0	11.6
5623334429462289992	139.043182373	−36.61378479	13.58	13.02	0.0	0.0	41.0	4.0	41.0	4.0
5623380270970381696	138.994445801	−36.629962921	16.55	15.80	51.0	3.7	0.0	0.0	51.0	3.7
5623334408586502656	139.035614014	−36.636032104	16.84	16.04	49.0	4.0	43.0	3.7	45.8	3.2
5623339077943312128	139.082473755	−36.624046326	15.88	15.21	202.0	22.3	173.0	18.0	184.5	16.5
5623339284101742592	139.076309204	−36.619358063	15.42	14.82	0.0	0.0	191.0	22.3	191.0	22.3
5623332309074877312	139.074935913	−36.679534912	15.00	14.49	92.0	12.8	0.0	0.0	92.0	12.8
5623322205995667456	139.064376831	−36.684459686	15.17	14.63	96.0	12.8	90.0	10.4	92.4	9.5
5623329996269657984	139.033828735	−36.681102753	15.83	15.18	0.0	0.0	177.0	16.2	177.0	16.2
5623380928105950720	138.946029663	−36.6171875	15.00	14.51	48.0	5.5	46.0	4.9	46.9	4.3
5623381340422800512	138.958129883	−36.58423996	14.94	14.51	59.0	8.6	57.0	7.3	57.8	6.6
5623386597462756480	139.006134033	−36.56627655	15.50	14.91	146.0	16.8	171.0	22.3	155.1	15.7
5623386597462754176	139.005584717	−36.557128906	15.64	15.03	159.0	18.4	144.0	19.9	152.1	16.0
5623386494383526400	139.068847656	−36.548202515	15.60	15.04	89.0	9.8	83.0	8.6	85.6	7.6
5623386837980904832	139.094543457	−36.540142059	16.01	15.28	133.0	11.0	124.0	12.5	129.1	9.8
5623338081510889344	139.144302368	−36.651504517	16.02	15.34	0.0	0.0	71.0	5.8	71.0	5.8
5623338253309593728	139.103302002	−36.649654388	15.14	14.55	0.0	0.0	205.0	23.6	205.0	23.6
5623380756307269120	138.918502808	−36.643554688	16.58	15.81	149.0	9.8	0.0	0.0	149.0	9.8
5623387422096548864	138.98815918	−36.52878952	15.66	15.04	171.0	21.1	152.0	17.4	159.7	15.8
5623387898833928448	139.043746948	−36.506778717	14.66	14.08	0.0	0.0	212.0	23.9	212.0	23.9
5623387078499074688	139.065994263	−36.520988464	15.88	15.18	196.0	18.7	0.0	0.0	196.0	18.7
5623386941060117760	139.107223511	−36.531391144	15.58	14.96	83.0	7.0	76.0	7.0	78.9	6.3
5623386941060118656	139.104309082	−36.534217834	16.21	15.48	73.0	5.5	55.0	4.6	62.4	4.2
5623338837425108864	139.16394043	−36.59770584	15.85	15.19	92.0	8.0	78.0	6.4	83.5	5.9
5623385528187471616	139.170883179	−36.626014709	16.42	15.62	0.0	0.0	136.0	9.5	136.0	9.5
5623380515789076992	138.987854004	−36.599262238	16.86	16.06	44.0	2.8	30.0	1.8	34.3	1.8
5623379824294763008	138.995162964	−36.658473969	17.13	16.28	40.0	3.7	37.0	3.1	38.2	2.8
5623380481429346304	138.972946167	−36.616920471	14.17	13.60	120.0	15.6	112.0	12.5	115.1	11.5
5623332893190448384	138.997970581	−36.663852692	14.31	13.85	116.0	17.7	107.0	13.8	110.4	12.7
5623380550148822144	138.969726562	−36.610404968	14.15	13.64	0.0	0.0	164.0	20.2	164.0	20.2
5623380378350116864	139.027633667	−36.602481842	15.96	15.31	71.0	6.1	0.0	0.0	71.0	6.1
5623380172191705600	138.955978394	−36.619419098	14.71	14.22	0.0	0.0	120.0	15.6	120.0	15.6
5623380309630647552	139.004837036	−36.616539001	16.09	15.29	0.0	0.0	82.0	5.2	82.0	5.2
5623380275270915840	138.986404419	−36.628726959	15.56	14.98	0.0	0.0	43.0	4.3	43.0	4.3
5623380412709857920	139.018722534	−36.610397339	15.10	14.57	190.0	30.9	0.0	0.0	190.0	30.9
5623380378350115840	139.033843994	−36.605182648	15.08	14.57	7.0	4.9	9.0	3.1	8.4	3.0
5623333305507291392	139.027664185	−36.642311096	14.72	14.36	80.9	13.5	0.0	0.0	80.9	13.5
5623380378350114816	139.034606934	−36.601577759	16.05	15.31	48.0	4.0	46.0	3.7	46.9	3.2
5623333236787821312	139.031326294	−36.661888123	15.34	14.72	245.0	31.2	0.0	0.0	245.0	31.2
5623379828594324608	138.987945557	−36.666103363	16.33	15.60	127.0	11.0	113.0	9.5	119.0	8.5
5623333133708811520	139.047271729	−36.655601501	15.97	15.30	114.0	9.8	0.0	0.0	114.0	9.8
5623333271147560960	139.010131836	−36.647571564	15.94	15.28	38.0	3.1	26.0	1.8	29.2	1.8

2.3 Extinction towards the cluster

The extinction towards the cluster was estimated by comparing the MIST (Choi et al. 2016) isochrones, at solar metallicity, to the observed CMD, at a fixed adopted distance (from the *Gaia* DR2 parallax). We allowed age to be a free parameter (between 100 Myr and 3 Gyr), and concentrated the fit on matching the main sequence (i.e. a region largely independent of the adopted age). We adopted the mean extinction coefficients for the *Gaia* filters from Casagrande & Vandenberg (2018), assuming $R_V = 3.1$. A_V was adjusted until the main sequence of the isochrones passed through the centre of the observed main sequence (between $16 \leq G_{BP} \leq 18$). We found that $A_V = 0.9 \pm 0.1$ mag provided the best fit to the data.

The result, however, is metallicity-dependent. Performing the same test with models of [Fe/H] = −0.5 led to a value of $A_V = 1.3$ mag. However, at this metallicity, the model isochrones displayed a curvature below the MSTO data that was not found in the observations. Hence, we adopt the value determined from the solar metallicity isochrones.

2.4 Cluster mass

We estimate the mass of the cluster by counting the number of stars within two magnitude intervals that should not be heavily affected by incompleteness or stellar evolution. We convert these magnitude intervals to mass, assuming an age of 800 Myr (see below), distance and extinction described above, and compare the number of observed stars with expectations from stochastically sampling from a Kroupa (2002) initial mass function. We find 57 and 28 stars within the mass intervals of 1.39–1.68 $M_\odot$ ($G_{BP} = 16–17$ mag) and 1.68–1.85 $M_\odot$ ($G_{BP} = 15.5–16$ mag), respectively. Comparing these numbers to 50 000 realizations of clusters with masses between 500 and 5000$M_\odot$, we find that the cluster initially contained 2400 ± 300 $M_\odot$ (not taking into account mass loss from tidal effects or two-body relaxation).

3 RESULTS

3.1 Extent of the eMSTO

As shown by Platais et al. (2012), differential extinction can mimic an eMSTO if not properly taken into account. A way to estimate the role of differential extinction is to look at the width of the main sequence. An example region is shown in the inset of the upper panel of Fig. 3, where we have fit a nominal ridge line to this section of the main sequence (solid line). We also show the same ridge line shifted by 0.01 magnitudes in colour in both directions, which encompasses most of the stars on the single-star main sequence. By applying different levels of extinction to the nominal ridge line (within the inset box in Fig. 3), we found that the amount of differential extinction present to be $A_V \leq 0.07$ mag, in order to stay within the 0.01 magnitude tolerance in colour.[6] Additionally, we see a sequence of binary stars well separated from the main sequence.

In the upper panel of Fig. 3, we overplot the MIST (Choi et al. 2016) isochrones for solar metallicity, and extinction value of $A_V = 0.9$, at the adopted distance. We plot a range of ages from log $t = 8.75...8.95$ (in steps of 0.05) that encompasses the width of the MSTO. Extrapolating between the outer isochrones, we see that

---

[6]This is smaller than the uncertainty in the absolute extinction towards the clusters because it is independent of the shape of the isochrone.
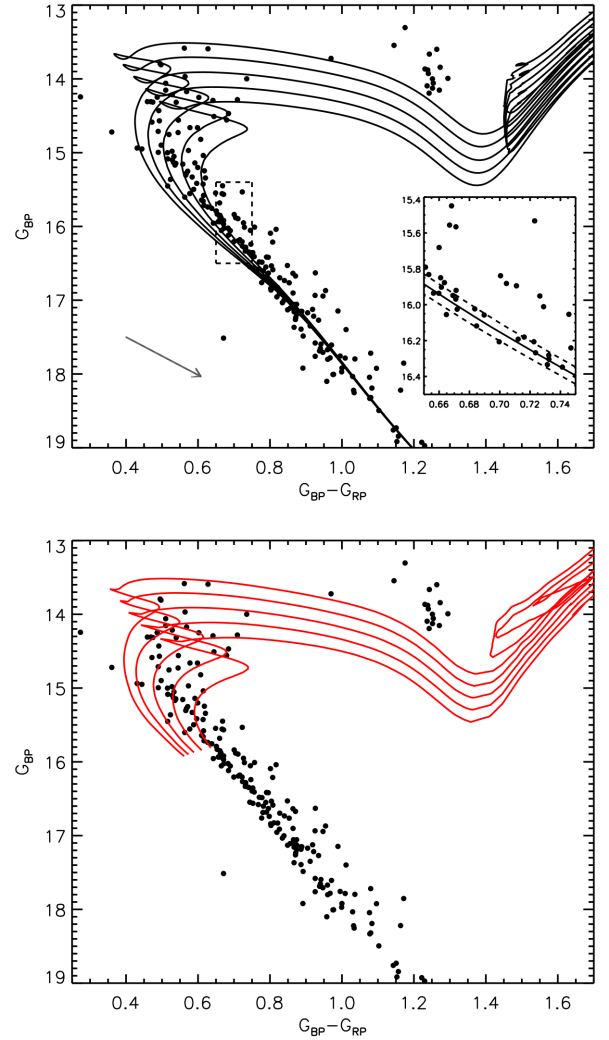
Figure 3. **Top panel:** The CMD (in *Gaia* passbands) of the cluster members based on the adopted selection criteria. The MIST isochrones (for standard models) for ages of log $t = 8.75...8.95$ (in steps of 0.05) are overplotted. The arrow shows the effect of $A_V = 0.5$ mag of extinction in the CMD. The dashed box is shown in more detail in the inset, where here the solid line is the nominal ridge line for the single-star MS and the dashed lines show the same line shifted by 0.01 magnitudes in colour. The narrowness of the MS indicates very little differential extinction is present. A binary sequence above the MS is clearly visible. **Bottom panel:** The same as the top panel but now for the Geneva isochrones with ages between log $t = 8.85...9.05$ (in steps of 0.05), for an initial rotation rate of $\Omega/\Omega_{c, initial} = 0.4$. The lowest mass stars in the isochrone is 1.7 $M_\odot$.

an age of log $t = 8.85$ fits the main part of the eMSTO (in agreement with previous age estimates – Mermilliod et al. 2001) with an inferred age spread between log $t = 8.775$ and 8.925 (∼245 Myr). More quantitatively, following on previous work (e.g. Goudfrooij et al. 2014; Niederhofer et al. 2016) we estimated the age of each star on the MSTO ($0.4 \leq G_{BP} − G_{RP} \leq 0.8$, $14 \leq G_{BP} \leq 15.5$) by finding the isochrone that passes closest to the star in the CMD (using isochrones with the same parameters as above and in steps of $\Delta(logage) = 0.01$). The mean age found with this method is 775 Myr with a dispersion of 120 Myr. We convert the estimated σ to FWHM in order to more directly compare with previous estimates, finding FWHM = 280 Myr, in good agreement with that found by eye.
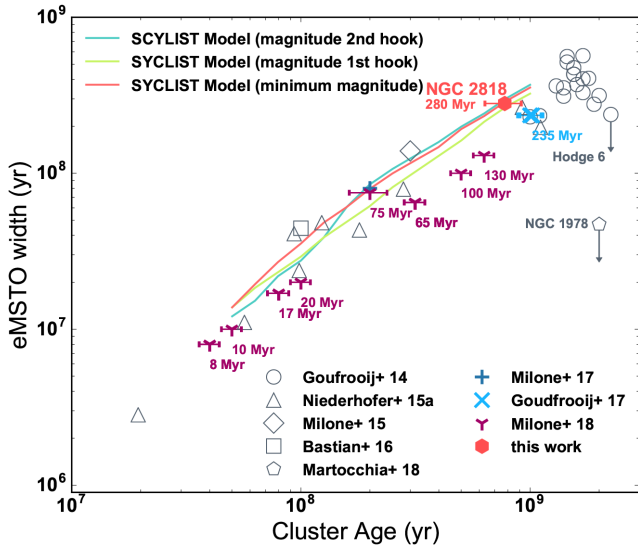
Figure 4. The relation between cluster age and inferred age spread for a sample of clusters from the literature as well as that found for NGC 2818 (see Niederhofer et al. 2015 for the original plot and a description of the models). We have added additional clusters from the literature in the past 3 yr (see text). NGC 2818 follows the trend found for other cluster samples. The horizontal 'error bars' for the Goudfrooij et al. (2017) and Milone et al. (2018) samples show, assuming the inferred age spreads are real, when star formation began and terminated within each cluster. Solid lines show the expectations for rotating stellar models (Niederhofer et al. 2015).

In the bottom panel of Fig. 3 we show the same analysis using the Geneva/SYCLIST isochrones using stellar models including rotation with an initial rotation rate of $\Omega/\Omega_{c,\,initial} = 0.4$ (Georgy et al. 2013a,b) with the same adopted parameters. We find that the two sets of isochrones give similar results, with the Geneva models giving slightly older ages, with a best-fitting age of log $t = 8.95$ and a spread of ~ 300 Myr.

We can compare the estimated age and inferred age spread with previous results in the literature. Niederhofer et al. (2015) showed that there exists a tight relation, as derived for LMC/SMC clusters, between the age of the cluster and the inferred age spread on the MSTO. The authors also showed that this is expected from models that included stellar rotation. In Fig. 4, we show an updated version of the Niederhofer et al. figure and highlight the position of NGC 2818. We also include recent results from Milone et al. (2015, 2016, 2018), Bastian et al. (2016), Goudfrooij, Girardi & Correnti (2017), and Martocchia et al. (2018). For the Milone et al. (2018) results, we adopt the difference between the ages of the non-rotating isochrone that fits the blue sequence and the rotating isochrone ($\Omega = 0.9$) that fits the red sequence.[7] For the Goudfrooij et al. (2017) results, we adopt the age difference between the two peaks of the pseudo-age distribution (their fig. 9).

The horizontal bars on the Milone et al. (2018) and Goudfrooij et al. (2017) represent the duration between when star-formation began and terminated, if the eMSTO is interpreted as an age spread.

---

[7] Note that this is different from the method used in all other referenced works in the current paper, and likely results in smaller age ranges that the other methods (as can be seen in Fig. 10 of Milone et al. 2018). This may explain why the Milone et al. (2018) data points are systematically below that found for other studies. However, a strong trend still exists between the age and inferred age spread for the clusters in their sample.

Note that if interpreted as an age spread, each cluster would begin and end to form stars at a different time. It would then need to be a coincidence that we observed each cluster at a very specific age in order to get the trend between age and age-spread.

Lines show the expected trend from stellar rotation as predicted by the Geneva/SYCLIST models (details below). The results for NGC 2818 nicely follow the same trend as previous results from the literature, although we note that the theoretical curves were calculated for LMC metallicity.

3.2 Comparison with stellar models with rotation

In order to address whether stellar rotation is the underlying cause of the eMSTO in NGC 2818, we have compared the observed CMD and $V\!\sin i$ measurements to predictions from the SYCLIST synthetic cluster models. For this, we have assumed an age of log t (yr) $= 8.95$, solar metallicity, a random inclination angle distribution, and a range of rotation rates from non-rotating to near-break-up ($\Omega/\Omega_{c,\,initial} = 0.95$). The models include gravity darkening (Espinosa Lara & Rieutord 2011) as well as geometric deformation at high rotational velocities (Georgy et al. 2014). We then determined the 5th and 95th percentiles in colour in 0.1-magnitude bins in G_{BP} over the range $13.5 \leq G_{BP} \leq 15.3$, to define blue and red ridge lines, respectively (see the top panel of Fig. 5). We then measured the normalized distance (in colour) to the blue ridgeline for every star brighter than $G_{BP} = 15.3$ (i.e. the MSTO).

The bottom panel of Fig. 5 presents the results where the points with error bars correspond to the observed stars in NGC 2818, while the grey crosses show the prediction from the models. At blue pseudo-colours, the observations show that the average $V\!\sin i$ is quite low and it significantly increases towards redder colours. This matches the expectations of the models.

4 DISCUSSION AND CONCLUSIONS

4.1 Mismatch between the observed and expected position of the red clump

A notable feature in Fig. 3 is the fact that the models do not reproduce the position of the red clump. We found that this holds for the MIST, Geneva, and Padova (Marigo et al. 2017) isochrones, independent of the metallicity adopted (even when allowing extinction to be a free parameter). If the distance is left as a free parameter, in addition to the age and extinction, an acceptable fit could be found. This suggests that there is either a problem in the calibration of the models for the red clump, or that the conversion between theoretical properties of the isochrones (temperature, gravity, and luminosity) to observational space in *Gaia* filters is off. Further observations of more open clusters, at different ages, should be able to differentiate between these possibilities.

4.2 The origin of the extended main sequence phenomenon

The discovery of an eMSTO in a low-mass ($\sim 2400\,M_\odot$), intermediate age (800–900 Myr) Galactic open cluster shows that the eMSTO phenomenon is not limited to high mass clusters, nor the special conditions of the LMC/SMC. Combining the clean CMD made possible from *Gaia* proper motions and parallaxes, with medium-resolution spectroscopy, shows that rapidly rotating stars are preferentially found on the red (cool) side of the MSTO, while slow rotators are found on the blue, nominal MSTO. Such a relation between colour
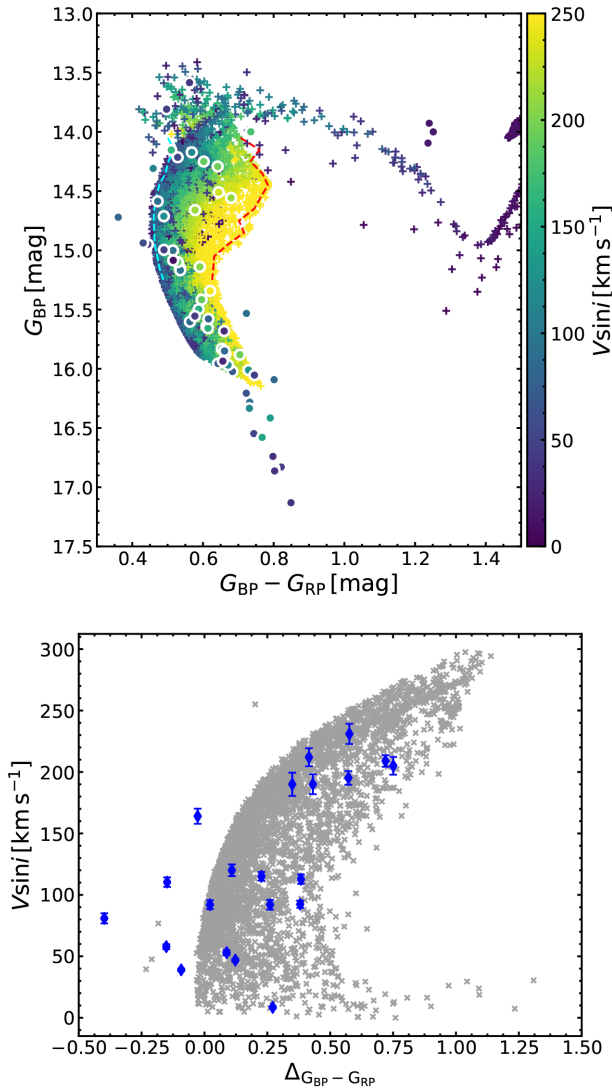
Figure 5. Top panel: The observed CMD of NGC 2818 members colour-coded by their measured $V\sin i$ values. The background coloured crosses show the predictions from the SYCLIST models, also colour-coded by their $V\sin i$ values. The adopted blue and red ridgelines are shown as dashed lines. **Bottom panel:** The $V\sin i$ value vs. the pseudo-colour (normalized colour difference from the blue ridgeline (top panel). We have only included stars with magnitudes brighter than $G_{BP} = 15.3$ (i.e. the MSTO) in the figure.

and rotational velocity ($V\sin i$) is expected from models that include stellar rotation.

In a future work, we will study a sample of open clusters available in the *Gaia* DR release to investigate the age – inferred age relation at solar metallicity (de Juan Ovelar et al., in prep.), and directly compare the observations to models that include magnetic breaking due to the onset of convection in lower mass stars (Georgy et al., in prep.).

REFERENCES

Bastian N., de Mink S. E., 2009, MNRAS, 398, L11
Bastian N., Lardo C., 2018, ARA&A, 56, preprint (arXiv:1712.01286)
Bastian N., et al., 2016, MNRAS, 460, L20
Bessell M. S., Castelli F., Plez B., 1998, A&A, 333, 231
Brandt T. D., Huang C. X., 2015a, ApJ, 807, 24
Brandt T. D., Huang C. X., 2015b, ApJ, 807, 25
Cabrera-Ziri I. et al., 2016, MNRAS, 457, 809
Casagrande L., VandenBerg D. A., 2018, MNRAS, 479, L102
Choi J., Dotter A., Conroy C., Cantiello M., Johnson B. D., 2016, ApJ, 823, 102
Conroy C., Spergel D. N., 2011, ApJ, 726, 36
Doyle A. P., Davies G. R., Smalley B., Chaplin W. J., Elsworth Y., 2014, MNRAS, 444, 3592
Dupree A. K. et al., 2017, ApJ, 846, L1
Espinosa Lara F., Rieutord M., 2011, A&A, 533, A43
Flower P. J., 1996, ApJ, 469, 355
Gaia Collaboration et al., 2016, A&A, 595, A1
Gaia Collaboration, Brown A. G. A., Vallenari A., Prusti T., de Bruijne J. H. J., Babusiaux C., Bailer-Jones C. A. L., 2018, A&A, preprint (arXiv:1804.09365)
Georgy C., Ekström S., Granada A., Meynet G., Mowlavi N., Eggenberger P., Maeder A., 2013a, A&A, 553, A24
Georgy C. et al., 2013b, A&A, 558, A103
Georgy C., Granada A., Ekström S., Meynet G., Anderson R. I., Wytten-bach A.., Eggenberger P., Maeder A., 2014, A&A, 566, A21
Goudfrooij P., et al., 2014, ApJ, 797, 35
Goudfrooij P., Girardi L., Correnti M., 2017, ApJ, 846, 22
Kamann S. et al., 2018, MNRAS, 580, 1689
Kroupa P., 2002, Science, 295, 82
Lindegren L. et al., 2018, A&A, 616, A2
Mackey A. D., Broby Nielsen P., 2007, MNRAS, 379, 151
Marigo P. et al., 2017, ApJ, 835, 77
Marino A. F., Przybilla N., Milone A. P., Da Costa G., D'Antona F., Dotter A., Dupree A., 2018, AJ, preprint (arXiv:1807.04493)
Martocchia S. et al., 2018, MNRAS, 477, 4696
Mermilliod J.-C., Clariá J. J., Andersen J., Piatti A. E., Mayor M., 2001, A&A, 375, 30
Milone A. P., Bedin L. R., Piotto G., Anderson J., 2009, A&A, 497, 755
Milone A. P. et al., 2015, MNRAS, 450, 3750
Milone A. P., Marino A. F., D'Antona F., Bedin L. R., Da Costa G. S., Jerjen H., Mackey A. D., 2016, MNRAS, 458, 4368
Milone A. P. et al., 2018, MNRAS, 477, 2640
Niederhofer F., Georgy C., Bastian N., Ekström S., 2015, MNRAS, 453, 2070

Niederhofer F., Bastian N., Kozhurina-Platais V., Hilker M., de Mink S. E., Cabrera-Ziri I., Li C., Ercolano B., 2016, A&A, 586, A148

Piatti A. E., Bastian N., 2016, A&A, 590, A50

Platais I. et al., 2012, ApJ, 751, L8

Sneden C., 1973, ApJ, 184, 839

Sneden C., Bean J., Ivans I., Lucatello S., Sobeck J., 2012, Astrophysics Source Code Library, ascl:1202.009

Stetson P. B., 2000, PASP, 112, 925

Torres G., 2010, AJ, 140, 1158

Tsantaki M., Sousa S. G., Adibekyan V. Zh., Santos N. C., Mortier A., Israelian G., 2013, A&A, 555, A150

Twarog B. A., 1983, ApJ, 267, 207

Twarog B. A., Anthony-Twarog B. J., Deliyannis C. P., Thomas D. T., 2015, AJ, 150, 134

SUPPORTING INFORMATION

Supplementary data are available at *MNRAS* online.

Table 1. Properties of the selected cluster candidate using the position, Plx and proper motions.

Please note: Oxford University Press is not responsible for the content or functionality of any supporting materials supplied by the authors. Any queries (other than missing material) should be directed to the corresponding author for the article.

This paper has been typeset from a TEX/LATEX file prepared by the author.